MoO_xS_y/Ni_3S_2 Microspheres on Ni Foam as Highly Efficient, Durable Electrocatalyst for Hydrogen Evolution Reaction

Zihuan Yu,[a] Huiqin Yao,[b] Yan Yang,[a,c] Mengwei Yuan,[a] Cheng Li,[d,*] Haiying He,[e,*] Ting-Shan Chan,[f] Dongpeng Yan,[a] Shulan Ma,[a,*] Peter Zapol,[g,*] and Mercouri G. Kanatzidis[c,g,*]

[a]*Beijing Key Laboratory of Energy Conversion and Storage Materials and College of Chemistry, Beijing Normal University, Beijing 100875, China. E-mail: mashulan@bnu.edu.cn*

[b]*School of Basic Medical Sciences, Ningxia Medical University, Yinchuan 750004, China.*

[c]*Department of Chemistry, Northwestern University, 2145 Sheridan Road, Evanston, IL 60208, USA. E-mail: m-kanatzidis@northwestern.edu*

[d]*Shanghai Institute of Applied Physics, Chinese Academy of Sciences, Shanghai 201800, China. E-mail: licheng@sinap.ac.cn*

[e]*Department of Physics and Astronomy, Valparaiso University, Valparaiso, IN 46383, USA. E-mail:haiying.he@valpo.edu*

[f]*National Synchrotron Radiation Research Center, 101 Hsin-Ann Road, Hsinchu Science Park, Hsinchu, 30076, Taiwan.*

[g]*Materials Science Division, Argonne National Laboratory, Lemont, IL 60439, USA. E-mail: Zapol@anl.gov*

ABSTRACT

Hydrogen energy derived from water splitting is the cleanest renewable energy source, but it is also very challenging to achieve because the hydrogen evolution reaction (HER) requires highly efficient and low-cost electrocatalysts. We fabricate a novel hierarchical system of amorphous molybdenum oxy/sulfide microspheres with crystalline Ni_3S_2 intergrown in situ on Ni foam ($MoO_xS_y/Ni_3S_2/NF$) as an outstanding electrocatalyst for HER. The $MoO_xS_y/Ni_3S_2/NF$ demonstrates ultra-low overpotential of 58 mV at current density of 10 mA cm^{-2} and extremely durable stability (>200 h), suggesting superior performance comparable to Pt-C/NF in acidic conditions. X-ray absorption fine structure (XAFS) determines the average valence state of Mo to be +(5+δ), with coordination motif by O and S. To explain such high HER activity, a $[Mo_2O_2(S,O)_4]$ dimer-based periodic model structure with average composition of $[Mo_4O_8S_4]$ interfaced with $Ni_3S_2(101)$ surface is proposed. The interactions between the Ni of Ni_3S_2 and bridging S/O of $[Mo_4O_8S_4]$ result in an average formal Mo charge state between +5 and +6, and significant charge transfer from Ni_3S_2 to $[Mo_4O_8S_4]$ activates the Mo=O bonds. The calculated $|\Delta G_{H^*}|$ of less than 50 meV suggests that the double bonded O is the most active site. This work points to the importance of oxy/sulfides with Mo^{n+} ($+5<n<+6$) as exceptional electrochemical catalysts for HER.

INTRODUCTION

With increasing demand for energy and gradual depletion of traditional fossil fuels, it is necessary to develop more sustainable and clean energy systems.[1] Hydrogen energy is the cleanest and most renewable energy source, and has been regarded as the most promising alternative.[2] Electrochemical splitting of water produces hydrogen via an important cathodic half reaction of hydrogen evolution reaction (HER).[3] However, high overpotentials and sluggish kinetics in HER impede efficient hydrogen generation from water.[4] Exceptional electrocatalysts are needed to reduce the overpotentials and accelerate hydrogen production rate.[5] Platinum (Pt) based materials are known as the most effective electrocatalysts towards HER,[6] while their high cost and unsatisfactory stability limit the large-scale applications. Thus, it is urgently needed to develop electrocatalysts with low cost, high efficiency, and high durability that replace platinum.

Researchers have made great efforts to investigate transition metal (such as Mo, Co, Ni, and Fe)-based electrocatalysts.[7] MoS_2 has been recognized as a promising HER electrocatalyst,[8] due to the optimal hydrogen adsorption energy on the edge sites.[9] However, catalytic performance of bulk MoS_2 is not ideal, because of poor intrinsic conductivity and limited number of active sites.[10, 11] Loading MoS_2 on conducting substrates, for example TiO_2,[12] metal foam[13] and carbon cloth,[4] has proven effective to increase the activity. To expose as many active sites as possible, versatile MoS_2 such as small-sized nanoparticles/nanosheets,[14, 15] vertically aligned nanofilms,[16] defect-rich nanosheets,[17] and mesoporous foams[18] have been developed. Our group reported MoS_2/Co_9S_8 nanosheets grown on nanorods of Ni_3S_2 supported on Ni foam (NF), fabricating a hierarchical co-assembly with abundant active sites beneficial to the enhancement of HER activity.[19] In addition, amorphous MoS_x (a-MoS_x) usually have HER-active defect sites on the surface, giving rise to attractive performance.[12, 20-22] At the same time, unsaturated sulfur atoms on the surface of MoS_x may participate in the discharge reactions and adsorb more hydrogen ions with favorable binding energies.[23] Chang *et al*. explained that the high HER efficiency of MoS_x is attributed to bridging S_2^{2-} and apical S^{2-}.[24] For synthesis of a-MoS_x, electrochemical deposition is the most

common method.[25] Using electrodeposition, Rees and coworkers prepared a-MoS_x thin films on Si/Ti/Au and investigated its inherent electrochemical features.[25] Wang *et al*. constructed polypyrrole(Ppy)/MoS_x films by electrochemical copolymerization of pyrrole and $(NH_4)_2MoS_4$.[26] Other routes such as precursor-thermolysis[24] were also developed, but simple and direct methods have rarely been exploited.

Molybdenum oxides (MoO_x), on the other hand, have been found to be electrocatalytically active toward HER. The α-MoO_3 nanobelts exhibited good HER performance requiring a 120 mV overpotential to achieve the current density of 10 mA cm^{-2} (η_{10}=120 mV).[27] Oxygen incorporation in crystalline MoS_2 was found to increase structure disorder, which offered more active sites beneficial to HER (η_{10}=180 mV).[28] In addition, molybdenum-oxo complex showed high stability and catalytic activity for HER.[29] Rees and coworkers revealed that the presence of Mo−O in AE-MoS_x (anodic electrode deposited a-MoS_x) played a key role in improving the HER performance.[25] However, easy preparation of well-defined molybdenum oxy/sulfides, especially in an amorphous state, is still challenging.

Here, we newly fabricate amorphous molybdenum oxy/sulfide microspheres with crystalline Ni_3S_2 intergrown in situ on NF, using a one-pot solvothermal reaction of Na_2MoO_4 and thiourea (CH_4N_2S) under the presence of cetyltrimethylammonium bromide (CTAB) (Figure 1a). The hierarchical MoO_xS_y/Ni_3S_2/NF structure demonstrates exceptional HER performance with an ultra-low overpotential (η_{10} = 58 mV) in acid media (0.5 M H_2SO_4) and dramatically durable stability (>200 h). X-ray absorption fine structure (XAFS) analyses reveal the valence of Mo in MoO_xS_y is +5.24, with the presence of Mo−O and Mo−S bonding. We note that this material is very different from the various MoS_x HER catalysts reported so far. In general, the reported a-MoS_x have mixed Mo oxidation states (with mainly Mo^{4+} and Mo^{6+}), and the coordination atoms of Mo are mainly S.[24, 26, 30] In our MoO_xS_y/Ni_3S_2, all Mo atoms have uniform oxidation state of +(5+δ). Moreover, each Mo is coordinated to terminal double-bonded O and bridging S/O atoms. Based on a broad battery of experimental evidence for the MoO_xS_y/Ni_3S_2 hierarchical structure, and the known structurally

established $[Mo_2S_2O_2]^{2+}$ dimer-based compounds,[31, 32] we propose a model structure with the repeating unit of $[Mo_4O_8S_4]$ to represent the key local structural characteristics of amorphous MoO_xS_y supported on the crystalline Ni_3S_2 structure. The $[Mo_4O_8S_4]$ chain-like structure features $[Mo_2O_2(S,O)_4]$ dimers with M=O bonding bridged by S or O atoms (see Figure S1). The bonding arrangement between $[Mo_4O_8S_4]$ and $Ni_3S_2(101)$ surface results in an average formal Mo charge state of +5.32. Density functional theory (DFT) calculations suggest that Mo=O unit is activated by the electron transfer from Ni_3S_2 to $[Mo_4O_8S_4]$, making the double bonded O the most active HER sites with the low free energy of hydrogen adsorption, $|\Delta G_H^*|$. The combination of these favourable characteristics of $[Mo_4O_8S_4]$ with the activating action of Ni_3S_2 and good electrical conductivity of the Ni_3S_2/NF support can explain the outstanding electrocatalytic performance.

EXPERIMENTAL SECTION

Synthesis of electrocatalyst samples. The electrocatalysts were synthesized *via* a simple one-step solvothermal reaction. $Na_2MoO_4 \cdot 2H_2O$ (2 mmol) and CTAB (2 mmol) were dissolved in an ethanol: water mixed solvent (1:1) to get a solution of 30 mL. After stirring for 15 min, 10 mmol of thiourea (CH_4N_2S) was dissolved in the above solution. The resulting solution was put into a Teflon-lined stainless-steel autoclave (50 mL) with immersing a piece of pre-treated NF. The autoclave was sealed and heated to certain temperature (160 and 180 °C) for 18 h. After cooled down, the products were taken out and rinsed with DI water and ethanol and dried in an oven at 45 °C for 12 h. Synthesis of other samples please see Supplementary Note 1. Characterization techniques are shown in Supplementary Note 2.

XAFS measurements. Mo L_3-edge XANES was recorded with a beamline 16A1 using total X-ray fluorescence yield (TFY) mode at the National Synchrotron Radiation Research Center (NSRRC), Hsinchu, Taiwan. Mo and Ni *K*-edges XAFS were collected in transmission mode at 1W1B endstation of Beijing synchrotron Radiation Facility and BL14W1 beamline of Shanghai Synchrotron Radiation Facility (SSRF). For details of

XAFS measurements and data fitting, see Supplementary Note 3.

Electrochemical measurements. Electrochemical measurements were performed in acidic solutions (0.5 M H_2SO_4) using a three-electrode system with the as-prepared substrate electrodes, Ag/AgCl (saturated KCl) and graphite electrode as working electrode, reference electrode and counter electrode, respectively. We cut the obtained samples with the size of 2 × 2 cm into two pieces of sample with the size of 1 × 2 cm, and kept the area immersed in the electrolyte at 1 × 1 cm during the electrochemical measurements. Details of electrochemical measurements are shown in Supplementary Note 4. Mass loadings of catalysts on NF were shown in Table S1.

DFT calculations. Based on the Mo-Mo dimer building block of $[Mo_2S_2O_2]^{2+}$,[31-32] structurally characterized polymeric chain of $[Mo_4O_8S_4]_n$[32] as a model for the local structure present in the MoO_xS_y was adopted. This model reproduces the local structure of the amorphous MoO_xS_y where the bridging O/S atoms are connected to the Ni_3S_2 support. The (101) and (110) surface orientations of Ni_3S_2 are adopted based on the orientations deduced from our HRTEM images. It is found that the (101) surface is energetically more stable than the (110) surface, consistent with previous computational studies.[33]

The two-electron HER can be modeled by two electrochemical reaction steps each with an ($H^+ + e^-$) pair transfer. The free energy change of each ($H^+ + e^-$) pair transfer reaction step was calculated using the computational hydrogen electrode (CHE) method.[34-36] The free energy was calculated by adding a Gibbs free energy correction[35] to the total energy calculated in VASP. The calculated free energy correction for H adsorption energy is 0.20 eV, fairly comparable to reported values.[37, 38] To identify the most active site, we have sampled multiple representative sites on the structure.

Other details involving DFT calculations, see Supplementary Note 5.

RESULTS AND DISCUSSION

Structural characterization. Products reacted at 160 °C and 180 °C with addition of 2 mmol CTAB are marked as 160-2CTAB and 180-2CTAB, while products reacted without CTAB are labeled as 160-no CTAB and 180-no CTAB. Figure 1a depicts the

formation process of 160-2CTAB. From Figure 1b and Figure S2, in all samples, regardless of CTAB addition, there are strong X-ray diffraction (XRD) peaks from Ni^0 of the NF substrate. Besides, a series of reflections at 2θ of 21.7°, 31.1°, 37.8°, 50.1° and 55.3° are assigned to (101), (110), (003), (211) and (300) planes of hexagonal Ni_3S_2,[19] which is generated *in-situ* from the reaction of HS^- with Ni^{2+} or the NF (Ni^0). No diffraction peaks related to MoS_x (or MoO_x) are detected in any of the samples. However, scanning electron microscopy-energy dispersive X-ray spectroscopy (SEM-EDX) analyses of 160-2CTAB (Figure S3) show the existence of Mo and S, suggesting the formation of Mo-based phases possibly in an amorphous form. At higher temperature of 180 °C (Figure S2), we found that the weak peak at around 2θ = 16° (marked with '■') could be observed in the product with CTAB (180-2CTAB), indicating the formation of crystalline MoS_2. For 180-no CTAB, the peak at about 16° is too weak to identify. While in the following XPS spectra we found the presence of Mo^{4+}, suggesting that the MoS_2 phase is still generated, although its content may be small.

Observations of morphology by SEM show that the 160-no CTAB (Figure 1c) grows into irregular particles, while 160-2CTAB (Figure 1d) presents regular microspheres (with a diameter of 2-3 μm). As the reaction temperature rises to 180 °C, microspheres with uneven size are formed (Figure S4). Transmission electron microscope (TEM) observations (Figure 1e-h) show that the average diameter of the 160-2CTAB microspheres is ~2 μm (Figure 1f), in agreement with the SEM results (Figure 1d). HRTEM images (Figure 1e,g) show interplanar spacings of 0.28 and 0.40 nm respectively ascribed to (110) and (101) planes of Ni_3S_2.[39] No distinguishable crystalline lattices of other phases are observed, suggesting the amorphous structure of the other substances. The interface between an amorphous phase and Ni_3S_2 phase can be clearly observed (Figure 1e, g). Elemental mapping indicates the existence of S and O besides Mo and Ni (Figure 1h), so we mark the amorphous phase as MoO_xS_y, and the 160-2CTAB as MoO_xS_y/Ni_3S_2/NF according to its composition.

The chemical valence of Mo was analysed by X-ray photoelectron spectroscopy

(XPS) (Figure 2a, b, d, e). For 160-2CTAB (Figure 2a), binding energies of 233.9 (Mo $3d_{3/2}$) and 230.7 (Mo $3d_{5/2}$) eV close to energy level of Mo^{5+} [7, 25, 40], suggesting an intermediate valence of Mo^{n+} ($4<n<6$). By contrast, at 180 °C, 180-2CTAB has two sets of peaks (Figure 2d), whose slightly larger energies of 234.1 and 230.9 eV indicate a higher valence of Mo^{m+} ($n<m<6$). Besides, the 232.4 and 229.2 eV energies assigned to Mo^{4+} $3d_{3/2}$ and Mo^{4+} $3d_{5/2}$ verify the formation of MoS_2[13, 19] at elevated temperature. If CTAB was absent in the reactions, the as-prepared 160-no CTAB (Figure 2b) presents only a pair of peaks at 235.6 and 232.4 eV related to Mo^{6+}, assigned mainly to MoS_4^{2-} rather than MoO_4^{2-} on the basis of Raman results discussed below. The presence of S in the products indicates that the starting material of thiourea decomposes to form HS^- ions and participates in the reactions. Here, the different valence of Mo between 160-2CTAB (~Mo^{5+}) and 160-no CTAB (Mo^{6+}) highlights the role of CTAB in controlling the redox process. From Figure 2e, for 180-no CTAB, besides the Mo^{6+} peaks (235.6 and 232.4 eV), there exists a pair of peaks at 232.0 and 228.8 eV assigned to Mo^{4+} of MoS_2.[41] This proves that higher temperature is conducive to MoS_2 generation. XPS data of S 2p (Figure S5) exhibit both S^{2-} and S_2^{2-} are present in all samples. From the Ni 2p shown in Figure S6, we observe all samples contain Ni^{2+}. Raman spectra (Figure 2c) of 160-2CTAB and 160-no CTAB indicate peaks ranging from 250 to 350 cm^{-1} belong to Mo−S modes.[25] Interestingly, obvious peaks at 800-950 cm^{-1} assigned to ν(Mo−O)[25, 42] are observed only in 160-2CTAB, confirming the significant presence of Mo−O bonds. FT-IR spectra (Figure 2f) depicts two distinguishing bands at 945 and 875 cm^{-1} ascribed to Mo=O and Mo−O, respectively.[40] The Mo=O data in IR are similar to those of dimeric species, such as $[Mo_2O_2(\mu\text{-}S)_2(S_2)(S_4)]^2$ (Mo=O at 925 cm^{-1})[43] and $[Mo_2O_2S_6]^{2-}$ (Mo=O at 928 cm^{-1}).[44]

To further probe the electronic state of Mo in MoO_xS_y and coordination environment, we analysed the X-ray absorption near edge structure (XANES). Figure 2g shows the shape of the L_3-edge in MoO_xS_y which is different from MoS_2 (Mo^{4+}) indicating that the oxidation state of Mo in MoO_xS_y is not +4. The Mo L_3-edges of MoO_xS_y and MoO_3 both depict a split doublet, which can be interpreted as a ligand field splitting of *d*-

orbitals.[45] The intensity of first peak (t_{2g} peak) decreases linearly with electron filling.[46] Compared with MoO_3 (Mo^{6+}), the weaker t_{2g} peak in MoO_xS_y implies the oxidation state of Mo is lower than +6. Figure 2h exhibits normalized Mo *K*-edge XANES spectra of MoO_xS_y and MoO_3 (Mo^{6+}) and MoS_2 (Mo^{4+}). The energy shift of the X-ray absorption edge originates from the change in oxidation state of Mo.[47] The energy of absorption edge for MoO_xS_y is higher than that of MoS_2 while lower than that of MoO_3 (Figure 2h inset), indicating oxidation state of Mo in MoO_xS_y is >4 and <6. The oxidation state of Mo can be derived from the energy shift of the X-ray absorption edge.[47] As shown in Figure 2i, we tested Mo *K*-edge XANES of Mo foil, MoS_2 and MoO_3, and the Mo average valence were obtained by use of the absorption edge.[48] From linear fitting of the valence state (see Figure 2i), the average Mo valence in MoO_xS_y is determined to be +5.24, which can be generalized to +(5+δ) given the amorphous nature of the material.

Extended X-ray absorption fine structure (EXAFS) analyses were performed to investigate coordination structure of Mo and local bond lengths.[49] As depicted in Figure 2j, good fitting of the Fourier transform (FT) in *R*-space is obtained. Table S2 indicates local structural parameters of the control samples of MoS_2, MoO_3 and MoO_xS_y. For MoS_2, the peak at 2.41 Å (phase shift uncorrected) corresponds to the Mo−S bond.[50] For MoO_3, the two main peaks at 1.74 Å and 1.96 Å correspond to $Mo-O_I$ and $Mo-O_{II}$ bonds, which are consistent with the reported Mo-O bond lengths of 1.7-2.2 Å.[51] For MoO_xS_y, the Mo−O distances are 1.68 ($Mo-O_I$) and 1.92 Å ($Mo-O_{II}$), and the Mo−S distance is 2.33 Å. The coordination numbers (CN) are 1.2, 1.7 and 2.0 related to $Mo-O_I$, $Mo-O_{II}$ and Mo−S, respectively. The slight difference in Mo−S and Mo−O distances in MoO_xS_y relative to MoS_2 and MoO_3 originates from different coordination motifs and oxidation state of Mo. The Mo−Mo distance ($d_{Mo\text{-}Mo}$) in MoO_xS_y is ~2.85 Å, much smaller than the distances in MoS_2 (d_{Mo-Mo} = 3.15 Å) and MoO_3 (d_{Mo-Mo} = 3.49 Å). It is noted that, the d_{Mo-Mo} of ~2.85 Å is very close to the value reported for dimeric clusters, such as $[Mo_2O_2S_6]^{2-}$ (d_{Mo-Mo} = 2.828 Å)[44] and $[Mo_2O_2(S)_2(S_2)_2]^{2-}$ (d_{Mo-Mo} = 2.825 Å).[52] The Ni K-edge XANES spectra of MoO_xS_y (MoO_xS_y/Ni_3S_2/NF) and

Ni_3S_2/NF are shown in Figure S7. This shows that the absorption edge of Ni in MoO_xS_y/Ni_3S_2/NF has an obvious shift to higher energy compared to Ni_3S_2/NF, suggesting that Ni electrons of Ni_3S_2 are delocalized after interfacing with MoO_xS_y.[53] This suggests that there would be electron transfer from Ni_3S_2 to MoO_xS_y moiety.

In order to provide physical insights for the high HER performance of such a system, we have adopted a polymeric structure deriving from the dimer units of $[Mo_2O_2(S,O)_4]$ (Figure S1) as a prototype to model the local structural characteristics of such amorphous MoO_xS_y in our DFT calculations. The proposed Mo^{5+} dimer structure model is based on the dimer core building block of $[Mo_2S_2O_2]^{2+}$ [31,38,46] and the related cyclic molecule of $[Mo_2S_2O_2(OH)_2]_6$.[32] As suggested by our HRTEM experiments (Figure 1e,g), both Ni_3S_2 (101) and (110) surfaces are exposed at the MoO_xS_y/Ni_3S_2 interfaces. We have considered both surface orientations, while the MoO_xS_y/Ni_3S_2(101) shows to have much better performance for HER activity. Hereafter, we will focus on the discussions of the MoO_xS_y/Ni_3S_2(101). As shown in Figure 2k, 2l, the $[Mo_4S_8O_4]$ unit is supported on the Ni_3S_2(101) surface, where both Ni-O and Ni-S bonds are formed (denoted as $[Mo_4O_8S_4]$@Ni_3S_2(101)), generating a heterojunction structure. Because of the difference in distances along the chain and distances between surface Ni atoms, some of the bridging oxygen atoms are unable to coordinate to the Ni atoms of the Ni_3S_2 structure, leading to a higher oxidation state of the nearest Mo ion. This model structure results in an average formal Mo charge state of 5.32, representing well the average Mo charge of ~5.24 obtained by XANES. The charge state above +5 causes some destabilization of the Mo-O double bonds, which become activated for H adsorption and hydrogen evolution that will be discussed below.

The calculated coordination numbers and bond distances are in agreement with the experimental values. The d_{Mo-Mo} is ~2.97 Å, about 4% longer than the measured value of 2.85 Å in the amorphous MoO_xS_y, but significantly shorter from the d_{Mo-Mo} values in MoS_2 (3.15 Å) and MoO_3 (3.49 Å), suggesting formation of Mo-Mo bond (via d^1-d^1 orbital interactions of Mo^{5+} atoms) similar to that observed in the reported molecular Mo dimers.[44, 52] The average distances are 1.67 Å for the Mo=O double bond (Mo−O_I,

CN=1), 1.98 Å for the Mo−O (bridging O) bond (Mo−O_{II}, CN=2), and 2.44 Å for Mo−S bond (CN=2). The d_{Mo-S} values vary slightly at different sites ranging 2.38~2.51 Å; while the $d_{Mo-O_{II}}$ values differ when the bridging O is bonded to surface Ni ($d_{Mo-O_{II}}$ = 2.03 Å) or not ($d_{Mo-O_{II}}$ = 1.93 Å).

Formation mechanism analysis. We analyze the reason for formation of spherical microstructure of MoO_xS_y/Ni_3S_2 as discussed in Supplementary Note 6. The proposed formation mechanism is described by Figure 1a and postulated in reactions 1-3. First, NH_2CSNH_2 decomposes to form HS^- ions (reaction 1) which reacts with Ni to produce Ni_3S_2 (reaction 2). At the same time, due to electrostatic interactions, positively-charged CTA^+ cations associate with MoO_4^{2-} anions forming the MoO_4-2CTA units in the form of micellar spherical vesicles (reaction 3). Then HS^- and MoO_4-2CTA engage in the sulfidation step. In general, the sulfidation requires an excess of sulfide species, while the vesicle, especially in its interior, provides a S-deficient environment. This prevents complete sulfidation, which possibly enables the retention of some Mo−O bonding, thus producing oxygen-rich MoO_xS_y (reaction 3). To explore the influence of substrates on products, we used carbon cloth (CC) instead of NF as substrate under the same reaction conditions. We found that there was almost no product grown on CC (Figure S8). This suggests the Ni_3S_2 generates preferentially on NF, providing a good second substrate favorable for the deposition of MoO_xS_y.

$$NH_2CSNH_2 + 3H_2O \rightarrow 2NH_4^+ + HS^- + HCO_3^- \quad (1)$$

$$3Ni + 2HS^- + 2H_2O \rightarrow Ni_3S_2 + 2OH^- + 2H_2 \quad (2)$$

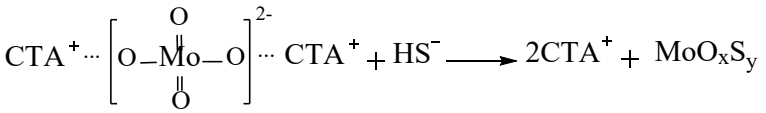

Electrocatalytic HER performance

The HER performance of 160-2CTAB and control samples was studied in an acid electrolyte (0.5 M H_2SO_4), with the results shown in Figure 3. Before the electrochemical test, 10 cycles of CV test was performed on all samples. The samples

grown in situ on NF were directly used as working electrodes. As shown in Figure 3a, the as-obtained 160-2CTAB shows an extremely low overpotential of 58 mV at the current density of 10 mA cm^{-2} (η_{10} = 58 mV), which is much lower than those of 160-no CTAB (η_{10}=128 mV) and Ni_3S_2/NF (η_{10} = 246 mV). The η_{10} value of 58 mV of 160-2CTAB approaches the Pt-C/NF (η_{10} = 43 mV) and Pt-C/GC (η_{10} = 36 mV, here GC is glass carbon electrode). For 180-2CTAB, the η_{10} of 86 mV is larger than 160-2CTAB, proving appropriate temperature is critical for improved HER activity. As summarized in Tables 1 and 2, HER activity of 160-2CTAB is comparable to or better than most reported Mo-/Ni- based electrocatalysts.[11, 24, 54-74] Remarkably, the ultra-low η_{10} value of 58 mV of 160-2CTAB points to its extremely attractive potential for HER.

The Tafel slope represents the intrinsic nature of an electrocatalyst and helps to understand rate determining steps in a reaction mechanism. The Tafel slope corresponds to one of three rate-determining steps (Volmer, Heyrovsky and Tafel) in the HER catalytic process.[75] Generally, a smaller Tafel slope suggests a faster reaction rate. As depicted in Figure 3b, 160-2CTAB has a slope of 43 mV/dec, near to Pt-C/NF (30 mV/dec), and much smaller than those of 160-no CTAB (136 mV/dec), 180-2CTAB (128 mV/dec, Figure S9b), and Ni_3S_2/NF (165 mV/dec). Based on the measured Tafel slopes, 160-no CTAB and 180-2CTAB are limited by the Volmer step, whereas 160-2CTAB is suggested to have the rate-limiting Heyrovsky step, and Pt-C adopts a rate-limiting Tafel step.[38] The smaller Tafel value of 160-2CTAB suggests that the reaction rate related to hydrogen adsorption (Volmer reaction, $H_3O^+ + e^- \rightarrow H_{ads} + H_2O$) is very fast, meaning that H_3O^+ is easily adsorbed on the surface of the catalyst. The exchange current density (j_0) is obtained by extrapolating the Tafel plot. From Figure S10, j_0 value of 160-2CTAB is 2.75 mA cm^{-2}, which is higher than the values of 160-no CTAB (2.00 mA cm^{-2}), Ni_3S_2/NF (0.32 mA cm^{-2}) and even higher than that of Pt-C/NF (2.31 mA cm^{-2}).

Electrochemical impedance spectroscopy (EIS) of 160-2CTAB shows a smaller diameter of semicircle than that of 160-no CTAB and Ni_3S_2/NF (Figure 3c). Thus, enhanced catalytic activity of 160-2CTAB over that of 160-no CTAB is demonstrated

by the significant reduction in the charge transfer resistance. The Nyquist plots and the charge-transfer resistance (R_{ct}) values were fitted by the equivalent circuit model (Figure S11). The 160-2CTAB shows a significantly decreased R_{ct} value (2.52 Ω), visibly smaller than 160-no CTAB (6.44 Ω) and Ni_3S_2/NF (21.65 Ω), suggesting a much faster charge transfer kinetics during the HER process (Table S3).

The electrochemically active surface area (ECSA) was evaluated through measuring the double layer capacitance (C_{dl}) in a non-faradaic region at different scan rates. The magnitude of C_{dl} indicates the number of active sites, which is a crucial factor affecting electrocatalytic performance. Figure 3d shows cyclic voltammograms of 160-2CTAB tested at varied scan rates (5, 10, 20, 40, 60 and 80 mV s^{-1}), and Figure 3e presents corresponding capacitive currents as a function of the scan rates, giving a C_{dl} of 81.5 mF cm^{-1}. As displayed in Figure S12, 180-2CTAB has a smaller C_{dl} value (45.0 mF cm^{-1}). The larger capacitance of 160-2CTAB indicates abundant active sites contributing to electrocatalytic activity. The Faradaic efficiency at a constant overpotential (-60 mV vs. RHE) in 0.5 M H_2SO_4 was measured by a home-made setup (Figure S13) to study the hydrogen conversion rate. The details on the testing of the Faradaic efficiency and related calculations are shown in Supplementary Note 7. Figure S14 displays the volume change of the produced H_2 at different time. The chronoamperometry curve taken at -60 mV is depicted in Figure S15. The good agreement of the experimentally generated and theoretically calculated amount of H_2 reveals a Faradaic efficiency of approximately 100% for the HER (Figure 3f and Table S4).

Stability is another important factor to evaluate the performance of catalysts. The time-dependent current density (I-t) of 160-2CTAB was monitored at constant potential of 120 mV and stayed basically constant under continuous operation for more than 200 h, suggesting superior stability (Figure 3g). At the initiation of the process, the current density of the 160-2CTAB increased gradually, and reached the maximum current density of 17.3 mA cm^{-2} at 15 h. In this stage (0-15 h), with increased electrolysis time, more electrolyte can access the nanointerface of the MoO_xS_y and Ni_3S_2, yielding an improved HER performance. Then the 160-2CTAB exhibited good stability under

continuous operation for the following 185 h. Finally, the catalyst retained nearly 99% current density after such a long time of electrolysis (17.3 mA cm^{-2} as maximum current density and 17.2 mA cm^{-2} as final current density). The inset of Figure 3g is the photograph showing generation of H_2 bubbles on the electrode. The video gives a visualized view of the large amounts of hydrogen produced during electrolysis (see Video S1). Figure 3h presents a partial enlargement of Figure 3g, clearly indicating accumulation-release process of the bubbles. The linear sweep voltammetry (LSV) curves of 160-2CTAB before and after I-t test were examined, and even after such a long test, there was little change in the overpotential at the same current density (Figure 3i). Also, the morphology of the 160-2CTAB well retained after 200 h of testing (Figure 3j,3k). XRD (Figure S16) and HRTEM (Figure S17) measurements confirmed the presence of crystalline Ni_3S_2 and amorphous phase, indicating the not significant change of the 160-2CTAB material after such long time (200 h) of HER testing. In order to verify the repeatability of the stability experiment, we conducted the stability test at a shorter time interval. As shown in Figure S18, the change trend of current density over the 50 h was similar to that of 200 h (Figure 3g). For this sample, we measured the XPS with corresponding analyses shown in Figure S19. As shown, after long-term HER reaction such as 50 h, the valence state of Ni and S did not change, while Mo presents mixed valence state of Mo^{5+}, Mo^{6+} and Mo^{4+}, in which the Mo^{5+} is the main component and the fraction of Mo^{6+} is relatively higher than that of Mo^{4+}. This suggests Mo^{5+} is disproportionated to form Mo^{6+} and Mo^{4+} during HER. To investigate if 160-2CTAB still exhibited long-term stability at a high current density, a chronoamperometric test was carried out at a potential of -300 mV (vs. RHE). Figure S20 showed that 160-2CTAB exhibited a high current density of 70 mA cm^{-2} without obvious attenuation for 50 h. All these indicated the exceptional stability of 160-2CTAB under low and high current density, suggesting an advanced electrocatalyst with prospects in devices based on HER in acidic media.

In order to study the chemical stability of the MoO_xS_y/Ni_3S_2/NF system in acidic conditions, we measured the dissolution rates of Mo and Ni during long-time

electrolysis of 60 h and even 200 h. From Table S5, in the first 60 h, the dissolution rate of Mo is higher than that of Ni, while within 200 h, the average dissolution rate of Ni becomes much higher than that of Mo. This result is consistent with our speculation about the formation mechanism of MoO_xS_y/Ni_3S_2. Since Ni_3S_2 is wrapped in MoO_xS_y, in the early stage of the electrolysis, the electrolyte mainly contacts with the exposed MoO_xS_y. As the electrolysis reaction goes on, the MoO_xS_y slowly dissolves, and the inwrapped Ni_3S_2 phase is gradually exposed to the solution. Because the Ni_3S_2 is more soluble in acidic solutions, giving a larger dissolution rate of Ni relative to Mo. In any case, the dissolution rates of Mo and Ni during 200 h electrolysis are only 30-50 ppb (μg/L)/h, indicating high chemical stability of the material. The much enhanced stability of Ni_3S_2 in acidic condition would be due to the envelop of Ni_3S_2 by the MoO_xS_y. At the same time, ultrasonication treatment was performed to confirm the mechanical stability of the MoO_xS_y/Ni_3S_2/NF (Figure S21), as shown no material loss occurred after ultrasonication in the solution for 30 min. The ultra-durable chemical/mechanical stability of MoO_xS_y/Ni_3S_2/NF is attributed to i) acid-resistant MoO_xS_y coating on Ni_3S_2 and ii) MoO_xS_y/Ni_3S_2 microspheres in situ growing on NF.

The balance of activity and stability of one catalyst can be defined by the ratio of the rate of hydrogen/oxygen production (current density *J*) to the rate of metal dissolution (equivalent dissolution current density, S). This activity-stability assessment is expressed as Activity-Stability Factor (ASF), described as Eq. (1).[76]

$$\mathrm{ASF} = \frac{J - S}{S}\Big|_{\eta} \qquad \text{(Eq. 1)}$$

Good catalyst normally have a high ASF value at constant overpotential (η). Evaluated by Eq. (1), the ASF value for 160-2CTAB is 43.47×10^3 (Table S6), being the largest among the reported samples, such as $MoS_2/Co_9S_8/Ni_3S_2$/Ni (ASF = 0.036×10^3 for HER in acid)[19] and dealloyed-thin-film $Ir_{25}Os_{75}$ (ASF = 20.67×10^3 for OER in acid).[76] The large ASF of the present 160-2CTAB material suggests an excellent balance between HER activity and stability.

Wettability results suggest that the MoO_xS_y system (160-2CTAB) has an optimum structure that facilitates the electrolyte entering the catalyst surface aiding the HER

performance in acidic solutions. The contact angle of bare NF was 127.3° (Figure S22a), indicating hydrophobicity. In contrast, as shown in Figure S22b, the water droplet entered the MoO_xS_y sample upon contact with the surface, meaning it is very hydrophilic.

Calculations of H adsorption free energy

DFT calculations can help to identify active sites and provide insights for the enhanced HER activity in the 160-2CTAB (Figure 4). Hydrogen adsorption free energy (ΔG_{H^*}) correlates with activity for HER.[4] Generally, an optimal electrocatalyst with high HER activity would have a $|\Delta G_{H^*}|$ close to zero. When $\Delta G_{H^*} > 0$, the binding force between catalyst and hydrogen is weak, and it is difficult to form a stable adsorption state of hydrogen (H_{ads}^*), thus the catalytic reaction is difficult to occur. When $\Delta G_{H^*} < 0$, the catalyst has strong adsorption for hydrogen, blocking the active sites from releasing hydrogen. We have computed ΔG_{H^*} at various binding sites of the $[Mo_4O_8S_4]$@Ni_3S_2(101) structural model (Figure 4A, 4C and Figure S23). The binding is more favourable at the double bonded O sites with the calculated $|\Delta G_{H^*}| \leq 0.05$ eV than the bridging S sites with the $|\Delta G_{H^*}| \leq 0.26$ eV, suggesting the computed overpotential for the Volmer step is no greater than 50 mV at pH=0. The corresponding HER free energy diagrams at a potential U = 0 V relative to the standard hydrogen electrode at pH=0 are shown in Figure S24. We have further analysed the charge population (see Bader charges in Figure 4B) and conducted interpolation to obtain the formal charge state for Mo (see Figure S25) with the resulting values of 5.26, 5.40, 5.41 and 5.22, for Mo1, Mo2, Mo3 and Mo4, respectively. Thereby, Mo atoms can be put into two groups: lower charge state around +5.24, where the Mo dimer is close to the Ni_3S_2 surface and the bridging O atoms are bonded to surface Ni; and higher charge state around +5.40 where the bridging O atoms in the Mo dimer are not bonded to the surface Ni. The lower-charge-state Mo sites are slightly exothermic in H adsorption with $\Delta G_{H^*} \approx -0.05$ eV, while the higher-charge-state Mo sites are slightly endothermic with $\Delta G_{H^*} \approx 0.01$-$0.03$ eV. It is notable, however, in both cases the formal charge state

of Mo is between +5 and +6 (i.e. +(5+δ)), in distinction from MoS_2 and MoO_3. Secondly, there is significant charge transfer (~1.10 e^-) from the Ni_3S_2 to the $[Mo_4O_8S_4]$ moiety consistent with XANES results, activating the Mo=O bonds. The $MoO_xS_y/Ni_3S_2(110)$ structural model was exhibited in Figure S26 and Figure S27. It is worth noting, however, that either too little charge transfer (case of $[Mo_4O_8S_4]@Ni_3S_2(110)$ with S termination ~0.62 e^-) or too much charge transfer (case of $[Mo_4O_8S_4]@Ni_3S_2(110)$ with Ni termination ~2.15 e^-) will deteoriate the HER performance. On the other hand, Ni_3S_2 is metallic and can better facilitate electron conductivity. For comparison, we have demonstrated that the standalone MoO_xS_y chain of $[Mo_6O_{12}S_6H_6]$, where all bridging oxygen atoms are fully coordinated by H (Figure S28) resulting in all Mo atoms in +5 state, is inert towards hydrogen adsorption. By removing a terminating H ($[Mo_6O_{12}S_6H_5]$), the average formal charge state of Mo increases to +5.17, leading to favourable H adsorption on oxygen in M=O bond (Figure S29). These results are consistent with those of our $[Mo_4O_8S_4]@Ni_3S_2(101)$ interface model. The Mo taking an intermediate state +(5+δ) can optimize the H adsorption, thus the HER reaction. Therefore, the chemical interactions of the MoO_xS_y and Ni_3S_2 play an important role in reducing the $|\Delta G_{H^*}|$, leading to the remarkable electrocatalytic performance of $MoO_xS_y/Ni_3S_2/NF$.

The present hierarchical $MoO_xS_y/Ni_3S_2/NF$ catalyst systems have four main advantages: i) the MoO_xS_y structure features Mo dimers and intermediate valence states of +(5+δ) for Mo ions, which are distinctly different from the known MoS_2 and MoO_3 materials; ii) the catalyst has primarily Mo=O as active sites, which are distinct from active sites known in MoS_2 and MoO_3 catalysts; iii) crystalline Ni_3S_2 helps to activate the catalytic function of MoO_xS_y by tuning H affinity of Mo=O via charge transfer; and iv) Ni substrate and metallic Ni_3S_2 both play an important role in facilitating electron conduction to the active sites.

CONCLUSION

A CTAB-controlled reaction chemistry creates a hierarchical $MoO_xS_y/Ni_3S_2/NF$

structure with unique structural characteristics and extremely high electrochemical stability in acidic media. The $MoO_xS_y/Ni_3S_2/NF$ displays outstanding HER performance in acid media, giving an extremely small overpotential (η_{10} = 58 mV) approaching that of Pt-C/NF (η_{10} = 43 mV). The catalyst exceeds both the activity and stability (>200h) of most known HER catalysts. The metallic Ni_3S_2, forms from partial sulfidation of NF and assists in activating the active sites of the amorphous MoO_xS_y catalyst featuring Mo atoms in average valence of +5.24 and a mixed coordination involving O and S. A dimer-based MoO_xS_y structure supported on the $Ni_3S_2(101)$ surface, namely $[Mo_4O_8S_4]@Ni_3S_2(101)$, is proposed as a model for the catalyst to provide insights for the observed catalytic activity. DFT calculations based on this structure model reproduce the Mo oxidation states, coordination numbers and bond distances as observed in the experiments. The DFT calculations suggest that the interactions of $[Mo_4O_8S_4]$ with the Ni_3S_2 effectively reduce the $|\Delta G_{H^*}|$ on the Mo=O unit, leading to the remarkable HER activity. Our findings suggest that Mo oxy/sulfides when hierarchically arranged on electron-rich supports such as the $MoO_xS_y/Ni_3S_2/NF$, can be superior to Mo sulfides. For exceptional electrochemical performance this work therefore provides new guidance to pursue mixed oxide/sulfide materials with Mo^{n+} oxidation state in the range $+5<n<+6$.

SSOCIATED CONTENT

Supporting Information

The Supporting Information is available free of charge at http://pubs.acs.org/XXX.

Supporting information: discussions of experimental details, SEM-EDX spectrum, XPS spectrum and SEM images, Ni K-edge XANES spectrum, polarization curves, Tafel slopes, cyclic voltammograms, equivalent circuit model, details on Faradaic efficiency test, contact angle photograph and droplet experiment of as-prepared samples, chronoamperometric curve, morphology and structure characterization after stability tests, some DFT calculation results, EXAFS curve-fitting results, parameters obtained by fitting the Nyquist plots, Faradaic efficiency of the produced H_2, dissolution rates of

metal ions of electrocatalyst, details of Activity-Stability Factor (ASF), average mass loading of catalysts on NF.

Video S1: Hydrogen produced during electrolysis.

AUTHOR INFORMATION

Corresponding Author

Shulan Ma - *Beijing Key Laboratory of Energy Conversion and Storage Materials and College of Chemistry, Beijing Normal University, Beijing 100875, China. E-mail: mashulan@bnu.edu.cn*

Mercouri G. Kanatzidis - *Department of Chemistry, Northwestern University, 2145 Sheridan Road, Evanston, IL 60208, USA. E-mail: m-kanatzidis@northwestern.edu*

Cheng Li - *Shanghai Institute of Applied Physics, Chinese Academy of Sciences, Shanghai 201800, China. E-mail: licheng@sinap.ac.cn*

Haiying He - *Department of Physics and Astronomy, Valparaiso University, Valparaiso, IN 46383, USA. E-mail: haiying.he@valpo.edu*

Peter Zapol - *Materials Science Division, Argonne National Laboratory, Lemont, IL 60439, USA. E-mail: Zapol@anl.gov*

Authors

Zihuan Yu - *Beijing Key Laboratory of Energy Conversion and Storage Materials and College of Chemistry, Beijing Normal University, Beijing 100875, China.*

Huiqin Yao - *School of Basic Medical Sciences, Ningxia Medical University, Yinchuan 750004, China.*

Yan Yang - *Beijing Key Laboratory of Energy Conversion and Storage Materials and College of Chemistry, Beijing Normal University, Beijing 100875, China.*

Mengwei Yuan - *Beijing Key Laboratory of Energy Conversion and Storage Materials and College of Chemistry, Beijing Normal University, Beijing 100875, China.*

Ting-Shan Chan - *National Synchrotron Radiation Research Center, 101 Hsin-Ann Road, Hsinchu Science Park, Hsinchu, 30076, Taiwan.*

Dongpeng Yan - *Beijing Key Laboratory of Energy Conversion and Storage Materials and College of Chemistry, Beijing Normal University, Beijing 100875, China.*

Notes

The authors declare no competing interests.

ACKNOWLEDGMENTS

Experimental work is supported by National Science Foundation of China (No. 22176017, U1832152, 11805261, and 21665021), Ministry of Science and Technology, Taiwan (Contract No. MOST 108-2113-M-213-006). Computational work was conducted at Argonne National Laboratory, a U.S. Department of Energy Office of Science laboratory, operated by UChicago Argonne, LLC under Contract no. DE-AC02-06CH11357. Use of the Center for Nanoscale Materials, an Office of Science user facility, was supported by the U.S. Department of Energy, Office of Science, Office of Basic Energy Sciences, under Contract No. DE-AC02-06CH11357. P.Z. and M.G.K. acknowledge support from the U.S. Department of Energy (DOE), Office of Science, Basic Energy Sciences, Materials Sciences and Engineering Division. We also acknowledge the beam time provided by 14W at Shanghai Synchrotron Radiation Facility (SSRF) and 1W1B endstation of Beijing Synchrotron Radiation Facility for the XAFS measurements.

REFERENCES

1. Chu, S.; Cui, Y.; Liu, N. The path towards sustainable energy. *Nat. Mater.* **2017,** *16* (1), 16-22.

2. Turner, J. A. Sustainable hydrogen production. *Science* **2004,** *305* (5686), 972-974.

3. Liu, C.; Ma, H.; Yuan, M.; Yu, Z.; Li, J.; Shi, K.; Liang, Z.; Yang, Y.; Zhu, T.; Sun, G.; Li, H.; Ma, S. (NiFe)S_2 nanoparticles grown on graphene as an efficient electrocatalyst for oxygen evolution reaction. *Electrochim. Acta* **2018,** *286*, 195-204.

4. Liu, Z.; Zhao, L.; Liu, Y.; Gao, Z.; Yuan, S.; Li, X.; Li, N.; Miao, S. Vertical nanosheet array of 1T phase MoS_2 for efficient and stable hydrogen evolution. *Appl. Catal. B* **2019,** *246*, 296-302.

5. Hu, J.; Zhang, C.; Meng, X.; Lin, H.; Hu, C.; Long, X.; Yang, S. Hydrogen evolution electrocatalysis with binary-nonmetal transition metal compounds. *J. Mater. Chem. A* **2017,** *5* (13), 5995-6012.

6. Strmcnik, D.; Lopes, P. P.; Genorio, B.; Stamenkovic, V. R.; Markovic, N. M. Design principles for hydrogen evolution reaction catalyst materials. *Nano Energy* **2016,** *29*, 29-36.

7. Tran, P. D.; Tran, T. V.; Orio, M.; Torelli, S.; Truong, Q. D.; Nayuki, K.; Sasaki, Y.; Chiam, S. Y.; Yi, R.; Honma, I.; Barber, J.; Artero, V. Coordination polymer structure and revisited hydrogen evolution catalytic mechanism for amorphous molybdenum sulfide. *Nat. Mater.* **2016,** *15* (6), 640-646.

8. Gao, M. R.; Liang, J. X.; Zheng, Y. R.; Xu, Y. F.; Jiang, J.; Gao, Q.; Li, J.; Yu, S. H. An efficient molybdenum disulfide/cobalt diselenide hybrid catalyst for electrochemical hydrogen generation. *Nat. Commun.* **2015,** *6*, 7.

9. F Jaramillo, T.; P Jørgensen, K.; Lindner Bonde, J.; H Nielsen, J.; Horch, S.; Chorkendorff, I. Identification of active edge sites for electrochemical H_2 evolution from MoS_2 nanocatalysts. Science **2007**, 317, 100-102.

10. Zhang, Z. Y.; Li, W. Y.; Yuen, M. F.; Ng, T. W.; Tang, Y. B.; Lee, C. S.; Chen, X. F.; Zhang, W. J., Hierarchical composite structure of few-layers MoS_2 nanosheets supported by vertical graphene on carbon cloth for high-performance hydrogen evolution reaction. *Nano Energy* **2015,** *18*, 196-204.

11. Kibsgaard, J.; Chen, Z.; Reinecke, B. N.; Jaramillo, T. F. Engineering the surface structure of MoS_2 to preferentially expose active edge sites for electrocatalysis. *Nat. Mater.* **2012,** *11* (11), 963-969.

12. Liu, Z.; Zhang, X.; Wang, B.; Xia, M.; Gao, S.; Liu, X.; Zavabeti, A.; Ou, J. Z.; Kalantar-Zadeh, K.; Wang, Y. Amorphous MoS_x-coated TiO_2 nanotube arrays for enhanced electrocatalytic hydrogen evolution reaction. *J. Phys. Chem. C* **2018,** *122* (24),

12589-12597.

13. Cao, J.; Zhou, J.; Zhang, Y.; Wang, Y.; Liu, X. Dominating role of aligned MoS_2/Ni_3S_2 nanoarrays supported on three-dimensional Ni foam with hydrophilic interface for highly enhanced hydrogen evolution reaction. *ACS Appl. Mater. Interfaces* **2018,** *10* (2), 1752-1760.

14. Li, Y.; Wang, H.; Xie, L.; Liang, Y.; Hong, G.; Dai, H. MoS_2 nanoparticles grown on graphene: an advanced catalyst for the hydrogen evolution reaction. *J. Am. Chem. Soc.* **2011,** *133* (19), 7296-7299.

15. Gao, M. R.; Chan, M. K. Y.; Sun, Y. G. Edge-terminated molybdenum disulfide with a 9.4-angstrom interlayer spacing for electrochemical hydrogen production. *Nat. Commun.* **2015,** *6*, 8.

16. Wang, H.; Lu, Z.; Xu, S.; Kong, D.; Cha, J. J.; Zheng, G.; Hsu, P. C.; Yan, K.; Bradshaw, D.; Prinz, F. B.; Cui, Y., Electrochemical tuning of vertically aligned MoS_2 nanofilms and its application in improving hydrogen evolution reaction. *Proc. Natl. Acad. Sci.* **2013,** *110* (49), 19701-19706.

17. Xie, J. F.; Zhang, H.; Li, S.; Wang, R. X.; Sun, X.; Zhou, M.; Zhou, J. F.; Lou, X. W.; Xie, Y. Defect-rich MoS_2 ultrathin nanosheets with additional active edge sites for enhanced electrocatalytic hydrogen evolution. *Adv. Mater.* **2013,** *25* (40), 5807-5813.

18. Deng, J.; Li, H. B.; Wang, S. H.; Ding, D.; Chen, M. S.; Liu, C.; Tian, Z. Q.; Novoselov, K. S.; Ma, C.; Deng, D. H.; Bao, X. H. Multiscale structural and electronic control of molybdenum disulfide foam for highly efficient hydrogen production. *Nat. Commun.* **2017,** *8*, 14430.

19. Yang, Y.; Yao, H.; Yu, Z.; Islam, S. M.; He, H.; Yuan, M.; Yue, Y.; Xu, K.; Hao, W.; Sun, G.; Li, H.; Ma, S.; Zapol, P.; Kanatzidis, M. G., Hierarchical nanoassembly of $MoS_2/Co_9S_8/Ni_3S_2$/Ni as a highly efficient electrocatalyst for overall water splitting in a wide pH range. *J. Am. Chem. Soc.* **2019,** *141* (26), 10417-10430.

20. Merki, D.; Fierro, S.; Vrubel, H.; Hu, X. L. Amorphous molybdenum sulfide films as catalysts for electrochemical hydrogen production in water. *Chem. Sci.* **2011,** *2* (7), 1262-1267.

21. Morales-Guio, C. G.; Hu, X. Amorphous molybdenum sulfides as hydrogen evolution catalysts. *Acc. Chem. Res.* **2014,** *47* (8), 2671-2681.

22. Weber, T.; Muijsers, J. C.; Niemantsverdriet, J. W. Structure of amorphous MoS_3. *J. Phys. Chem.* **1995,** *99* (22), 9194-9200.

23. Dinda, D.; Ahmed, M. E.; Mandal, S.; Mondal, B.; Saha, S. K. Amorphous molybdenum sulfide quantum dots: an efficient hydrogen evolution electrocatalyst in neutral medium. *J. Mater. Chem. A* **2016,** *4* (40), 15486-15493.

24. Chang, Y. H.; Lin, C. T.; Chen, T. Y.; Hsu, C. L.; Lee, Y. H.; Zhang, W.; Wei, K. H.; Li, L. J. Highly efficient electrocatalytic hydrogen production by MoS_x grown on graphene-protected 3D Ni foams. *Adv. Mater.* **2013,** *25* (5), 756-760.

25. Escalera-López, D.; Lou, Z.; Rees, N. V. Benchmarking the activity, stability, and inherent electrochemistry of amorphous molybdenum sulfide for hydrogen production. *Adv. Energy Mater.* **2019,** *9* (8), 1802614.

26. Wang, T.; Zhuo, J.; Du, K.; Chen, B.; Zhu, Z.; Shao, Y.; Li, M. Electrochemically fabricated polypyrrole and MoS_x copolymer films as a highly active hydrogen evolution electrocatalyst. *Adv. Mater.* **2014,** *26* (22), 3761-3766.

27. Sinaim, H.; Ham, D. J.; Lee, J. S.; Phuruangrat, A.; Thongtem, S.; Thongtem, T. Free-polymer controlling morphology of α-MoO_3 nanobelts by a facile hydrothermal synthesis, their electrochemistry for hydrogen evolution reactions and optical properties. *J. Alloys Compd.* **2012,** *516*, 172-178.

28. Xie, J.; Zhang, J.; Li, S.; Grote, F.; Zhang, X.; Zhang, H.; Wang, R.; Lei, Y.; Pan, B.; Xie, Y. Controllable disorder engineering in oxygen-incorporated MoS_2 ultrathin nanosheets for efficient hydrogen evolution. *J. Am. Chem. Soc.* **2013,** *135* (47), 17881-17888.

29. Karunadasa, H. I.; Chang, C. J.; Long, J. R. A molecular molybdenum-oxo catalyst for generating hydrogen from water. *Nature* **2010,** *464* (7293), 1329-1333.

30. Yang, P.; Wang, B.; Liu, Z. Q. Towards activation of amorphous MoS_x via Cobalt doping for enhanced electrocatalytic hydrogen evolution reaction. *Int. J. Hydrog. Energy* **2018,** *43* (52), 23109-23117.

31. Cadot, E.; Sokolov, M. N.; Fedin, V. P.; Simonnet-Jegat, C.; Floquet, S.; Secheresse, F. A building block strategy to access sulfur-functionalized polyoxometalate based systems using $\{Mo_2S_2O_2\}$ and $\{Mo_3S_4\}$ as constitutional units, linkers or templates. *Chem. Soc. Rev.* **2012,** *41* (22), 7335-7353.

32. Cadot, E.; Salignac, B.; Halut, S.; Secheresse, F. $[Mo_{12}S_{12}O_{12}(OH)_{12}(H_2O)_6]$: A cyclic molecular cluster based on the $[Mo_2S_2O_2]^{2+}$ building block. *Angew. Chem. Int. Edit.* **1998,** *37* (5), 611-612.

33. Zhang, B.; Fu, X. L.; Song, L.; Wu, X. J. Surface selectivity of Ni_3S_2 toward hydrogen evolution reaction: a first-principles study. *Phys. Chem. Chem. Phys.* **2020,** *22* (44), 25685-25694.

34. Nørskov, J. K.; Rossmeisl, J.; Logadottir, A.; Lindqvist, L.; Kitchin, J. R.; Bligaard, T.; Jónsson, H. Origin of the overpotential for oxygen reduction at a fuel-cell cathode. *J. Phys. Chem. B* **2004,** *108* (46), 17886-17892.

35. Peterson, A. A.; Abild-Pedersen, F.; Studt, F.; Rossmeisl, J.; Norskov, J. K. How copper catalyzes the electroreduction of carbon dioxide into hydrocarbon fuels. *Energy Environ Sci.* **2010,** *3* (9), 1311-1315.

36. Peterson, A. A.; Nørskov, J. K. Activity descriptors for CO_2 electroreduction to methane on transition-metal catalysts. *J. Phys. Chem. Lett.* **2012,** *3* (2), 251-258.

37. Hinnemann, B.; Moses, P. G.; Bonde, J.; Jørgensen, K. P.; Nielsen, J. H.; Horch, S.; Chorkendorff, I.; Nørskov, J. K. Biomimetic hydrogen evolution: MoS_2 nanoparticles as catalyst for hydrogen evolution. *J. Am. Chem. Soc.* **2005,** *127* (15), 5308-5309.

38. Jiao, Y.; Zheng, Y.; Davey, K.; Qiao, S.-Z. Activity origin and catalyst design principles for electrocatalytic hydrogen evolution on heteroatom-doped graphene. *Nature Energy* **2016,** *1* (10).

39. Zhou, W.; Wu, X.-J.; Cao, X.; Huang, X.; Tan, C.; Tian, J.; Liu, H.; Wang, J.; Zhang, H. Ni_3S_2 nanorods/Ni foam composite electrode with low overpotential for electrocatalytic oxygen evolution. *Energy Environ. Sci.* **2013,** *6* (10), 2921-2924.

40. Weber, T.; Muijsers, J. C.; vanWolput, H.; Verhagen, C. P. J.; Niemantsverdriet, J. W. Basic reaction steps in the sulfidation of crystalline MoO_3 to MoS_2 as studied by X-

ray photoelectron and infrared emission spectroscopy. *J. Phys. Chem.* **1996,** *100* (33), 14144-14150.

41. Pham, K. C.; Chang, Y. H.; McPhail, D. S.; Mattevi, C.; Wee, A. T.; Chua, D. H. Amorphous molybdenum sulfide on graphene-carbon nanotube hybrids as highly active hydrogen evolution reaction catalysts. *ACS Appl. Mater. Interfaces* **2016,** *8* (9), 5961-5971.

42. Daeneke, T.; Dahr, N.; Atkin, P.; Clark, R. M.; Harrison, C. J.; Brkljaca, R.; Pillai, N.; Zhang, B. Y.; Zavabeti, A.; Ippolito, S. J.; Berean, K. J.; Ou, J. Z.; Strano, M. S.; Kalantar-Zadeh, K. Surface water dependent properties of sulfur-rich molybdenum sulfides: electrolyteless gas phase water splitting. *ACS nano* **2017,** *11* (7), 6782-6794.

43. McAllister, J.; Bandeira, N. A. G.; McGlynn, J. C.; Ganin, A. Y.; Song, Y. F.; Bo, C.; Miras, H. N. Tuning and mechanistic insights of metal chalcogenide molecular catalysts for the hydrogen-evolution reaction. *Nat Commun* **2019,** *10* (1), 370.

44. Coucouvanis, D.; Toupadakis, A.; Hadjikyriacou, A. Synthsis of thiomolybdenyl complexs with $Mo_2(S)_2(O)_2^{2+}$ cores and molecular-structure of the $Mo_2O_2S_4(DMF)_3$ complex. *Inorg. Chem.* **1988,** *27* (19), 3272-3273.

45. Bare, S. R.; Mitchell, G. E.; Maj, J. J.; Vrieland, G. E.; Gland, J. L. Local site symmetry of dispersed molybdenum oxide catalysts-XANES at the Mo $L_{2,3}$-edges. *J. Phys. Chem.* **1993,** *97* (22), 6048-6053.

46. Degroot, F. M. F.; Hu, Z. W.; Lopez, M. F.; Kaindl, G.; Guillot, F.; Tronc, M. Differences between L_3 and L_2 X-ray-absorption spectra of transition-metal compounds. *J. Chem. Phys.* **1994,** *101* (8), 6570-6576.

47. Ebbinghaus, S.; Hu, Z.; Reller, A. Determination of the oxidation states of Cu and Ru in the system $La_{2-x}Sr_xCu_{1-y}Ru_yO_{4-\delta}$ by XANES-measurements. *J. Solid State Chem.* **2001,** *156* (1), 194-202.

48. Ressler, T.; Jentoft, R. E.; Wienold, J.; Gunter, M. M.; Timpe, O. In situ XAS and XRD studies on the formation of Mo suboxides during reduction of MoO_3. *J. Phys. Chem. B* **2000,** *104* (27), 6360-6370.

49. Yang, S.; Zhang, K.; Wang, C. D.; Zhang, Y. K.; Chen, S. M.; Wu, C. Q.; Vasileff,

A.; Qiao, S. Z.; Song, L. Hierarchical 1T-MoS_2 nanotubular structures for enhanced supercapacitive performance. *J. Mater. Chem. A* **2017,** *5* (45), 23704-23711.

50. Lassalle-Kaiser, B.; Merki, D.; Vrubel, H.; Gul, S.; Yachandra, V. K.; Hu, X.; Yano, J. Evidence from in situ X-ray absorption spectroscopy for the involvement of terminal disulfide in the reduction of protons by an amorphous molybdenum sulfide electrocatalyst. *J. Am. Chem. Soc.* **2015,** *137* (1), 314-321.

51. Mao, J. J.; Chen, W. X.; He, D. S.; Wan, J. W.; Pei, J. J.; Dong, J. C.; Wang, Y.; An, P. F.; Jin, Z.; Xing, W.; Tang, H. L.; Zhuang, Z. B.; Liang, X.; Huang, Y.; Zhou, G.; Wang, L. Y.; Wang, D. S.; Li, Y. D. Design of ultrathin Pt-Mo-Ni nanowire catalysts for ethanol electrooxidation. *Sci. Adv.* **2017,** *3* (8), 9.

52. Rittner, W.; Muller, A.; Neumann, A.; Bather, W.; Sharma, R. C. Generation of the triangulo-group Mo^{V}-η-S_2 in the condensation of $[Mo^{IV}O_2S_2]$ to $[Mo_2{}^{V}O_2S_2(S_2)_2]^2$. Angew. Chem. Int. Edit. Engl. **1979,** *18* (7), 530-531.

53. Kubobuchi, K.; Mogi, M.; Matsumoto, M.; Baba, T.; Yogi, C.; Sato, C.; Yamamoto, T.; Mizoguchi, T.; Imai, H. A valence state evaluation of a positive electrode material in an Li-ion battery with first-principles K- and L-edge XANES spectral simulations and resonance photoelectron spectroscopy. *J. Appl. Phys.* **2016,** *120* (14), 142125.

54. Xie, J.; Zhang, H.; Li, S.; Wang, R.; Sun, X.; Zhou, M.; Zhou, J.; Lou, X. W.; Xie, Y. Defect-rich MoS_2 ultrathin nanosheets with additional active edge sites for enhanced electrocatalytic hydrogen evolution. Adv. Mater. **2013,** *25* (40), 5807-5813.

55. Benck, J. D.; Chen, Z.; Kuritzky, L. Y.; Forman, A. J.; Jaramillo, T. F. Amorphous molybdenum sulfide catalysts for electrochemical hydrogen production: insights into the origin of their catalytic activity. *ACS Catal.* **2012,** *2* (9), 1916-1923.

56. Kibsgaard, J.; Jaramillo, T. F.; Besenbacher, F., Building an appropriate active-site motif into a hydrogen-evolution catalyst with thiomolybdate $[Mo_3S_{13}]^{2-}$ clusters. *Nat. Chem.* **2014,** *6* (3), 248-253.

57. Li, D. J.; Maiti, U. N.; Lim, J.; Choi, D. S.; Lee, W. J.; Oh, Y.; Lee, G. Y.; Kim, S. O. Molybdenum sulfide/N-doped CNT forest hybrid catalysts for high-performance hydrogen evolution reaction. *Nano lett.* **2014,** *14* (3), 1228-1233.

58. Merki, D.; Vrubel, H.; Rovelli, L.; Fierro, S.; Hu, X. Fe, Co, and Ni ions promote the catalytic activity of amorphous molybdenum sulfide films for hydrogen evolution. *Chem. Sci.* **2012,** *3* (8), 2515.

59. Chia, X.; Sutrisnoh, N. A. A.; Pumera, M. Tunable Pt-MoS_x hybrid catalysts for hydrogen evolution. *ACS Appl. Mater. Interfaces* **2018,** *10* (10), 8702-8711.

60. Tan, S. M.; Pumera, M. Composition-graded $MoWS_x$ hybrids with tailored catalytic activity by bipolar electrochemistry. *ACS Appl. Mater. Interfaces* **2017,** *9* (48), 41955-41964.

61. Shi, Y.; Wang, J.; Wang, C.; Zhai, T. T.; Bao, W. J.; Xu, J. J.; Xia, X. H.; Chen, H. Y. Hot electron of Au nanorods activates the electrocatalysis of hydrogen evolution on MoS_2 nanosheets. *J. Am. Chem. Soc.* **2015,** *137* (23), 7365-7370.

62. Han, X.; Tong, X.; Liu, X.; Chen, A.; Wen, X.; Yang, N.; Guo, X.-Y. Hydrogen evolution reaction on hybrid catalysts of vertical MoS_2 nanosheets and hydrogenated graphene. *ACS Catal.* **2018,** *8* (3), 1828-1836.

63. Lukowski, M. A.; Daniel, A. S.; Meng, F.; Forticaux, A.; Li, L.; Jin, S. Enhanced hydrogen evolution catalysis from chemically exfoliated metallic MoS_2 nanosheets. *J. Am. Chem. Soc.* **2013,** *135* (28), 10274-10277.

64. Staszak-Jirkovsky, J.; Malliakas, C. D.; Lopes, P. P.; Danilovic, N.; Kota, S. S.; Chang, K. C.; Genorio, B.; Strmcnik, D.; Stamenkovic, V. R.; Kanatzidis, M. G.; Markovic, N. M. Design of active and stable Co-Mo-S_x chalcogels as pH-universal catalysts for the hydrogen evolution reaction. *Nat. Mater.* **2016,** *15* (2), 197-203.

65. Liu, P. T.; Zhu, J. Y.; Zhang, J. Y.; Xi, P. X.; Tao, K.; Gao, D. Q.; Xue, D. S. P dopants triggered new basal plane active sites and enlarged interlayer spacing in MoS_2 nanosheets toward electrocatalytic hydrogen evolution. *ACS Energy Lett.* **2017,** *2* (4), 745-752.

66. Zhou, Y.; Li, T. T.; Xi, S. Q.; He, C.; Yang, X. G.; Wu, H. J. One-step synthesis of self-standing Ni_3S_2/Ni_2P heteronanorods on nickel foam for efficient electrocatalytic hydrogen evolution over a wide pH range. *ChemCatChem* **2018,** *10* (23), 5487-5495.

67. Yu, J.; Ma, F. X.; Du, Y.; Wang, P. P.; Xu, C. Y.; Zhen, L. In situ growth of Sn-

doped Ni_3S_2 nanosheets on Ni foam as high-performance Electrocatalyst for hydrogen evolution reaction. *ChemElectroChem* **2017,** *4* (3), 594-600.

68. Sun, M. J.; Zhang, Z. Y.; Wang, Z.; Wang, S. J.; Zhang, S. Y.; Wang, R. T.; Song, X. C. Plasma-assisted synthesis of 3D hierarchical Ni_2P on Ni foam as highly active hydrogen evolution reaction electrocatalysts. *Int. J. Electrochem. Sci.* **2020,** *15* (10), 9734-9745.

69. Wang, K. W.; She, X. L.; Chen, S.; Liu, H. L.; Li, D. H.; Wang, Y.; Zhang, H. W.; Yang, D. J.; Yao, X. D. Boosting hydrogen evolution via optimized hydrogen adsorption at the interface of CoP_3 and Ni_2P. *J. Mater. Chem. A* **2018,** *6* (14), 5560-5565.

70. Yan, L. T.; Dai, P. C.; Wang, Y.; Gu, X.; Li, L. J.; Cao, L.; Zhao, X. B. In situ synthesis strategy for hierarchically porous Ni_2P polyhedrons from MOFs templates with enhanced electrochemical properties for hydrogen evolution. *ACS Appl. Mater. Interfaces* **2017,** *9* (13), 11642-11650.

71. Do, H.; Le, Q. V.; Lee, T. H.; Hong, S. H.; Ahn, S. H.; Jang, H. W.; Kim, S. Y. Core-shell architecture of $NiSe_2$ nanoparticles@nitrogen-doped carbon for hydrogen evolution reaction in acidic and alkaline media. *Int. J. Energy Res.* **2021**, *45* (14), 20463-20473.

72. Kwak, I. H.; Im, H. S.; Jang, D. M.; Kim, Y. W.; Park, K.; Lim, Y. R.; Cha, E. H.; Park, J. $CoSe_2$ and $NiSe_2$ nanocrystals as superior bifunctional catalysts for electrochemical and photoelectrochemical water splitting. *ACS Appl. Mater. Interfaces* **2016,** *8* (8), 5327-5334.

73. Zhou, H. Q.; Wang, Y. M.; He, R.; Yu, F.; Sun, J. Y.; Wang, F.; Lan, Y. C.; Ren, Z. F.; Chen, S. One-step synthesis of self-supported porous $NiSe_2$/Ni hybrid foam: An efficient 3D electrode for hydrogen evolution reaction. *Nano Energy* **2016,** *20*, 29-36.

74. Li, W. X.; Yu, B.; Hu, Y.; Wang, X. Q.; Yang, D. X.; Chen, Y. F., Core-shell structure of $NiSe_2$ nanoparticles@nitrogen-doped graphene for hydrogen evolution reaction in both acidic and alkaline media. *ACS Sustain. Chem. Eng.* **2019,** *7* (4), 4351-4359.

75. Luo, Z.; Miao, R.; Huan, T. D.; Mosa, I. M.; Poyraz, A. S.; Zhong, W.; Cloud, J. E.; Kriz, D. A.; Thanneeru, S.; He, J.; Zhang, Y.; Ramprasad, R.; Suib, S. L.

Mesoporous MoO_{3-x} material as an efficient electrocatalyst for hydrogen evolution reactions. *Adv. Energy Mater.* **2016,** *6* (16), 1600528.

76. Kim, Y. T.; Lopes, P. P.; Park, S. A.; Lee, A. Y.; Lim, J.; Lee, H.; Back, S.; Jung, Y.; Danilovic, N.; Stamenkovic, V.; Erlebacher, J.; Snyder, J.; Markovic, N. M. Balancing activity, stability and conductivity of nanoporous core-shell iridium/iridium oxide oxygen evolution catalysts. *Nat. Commun.* **2017,** *8* (1), 1449.

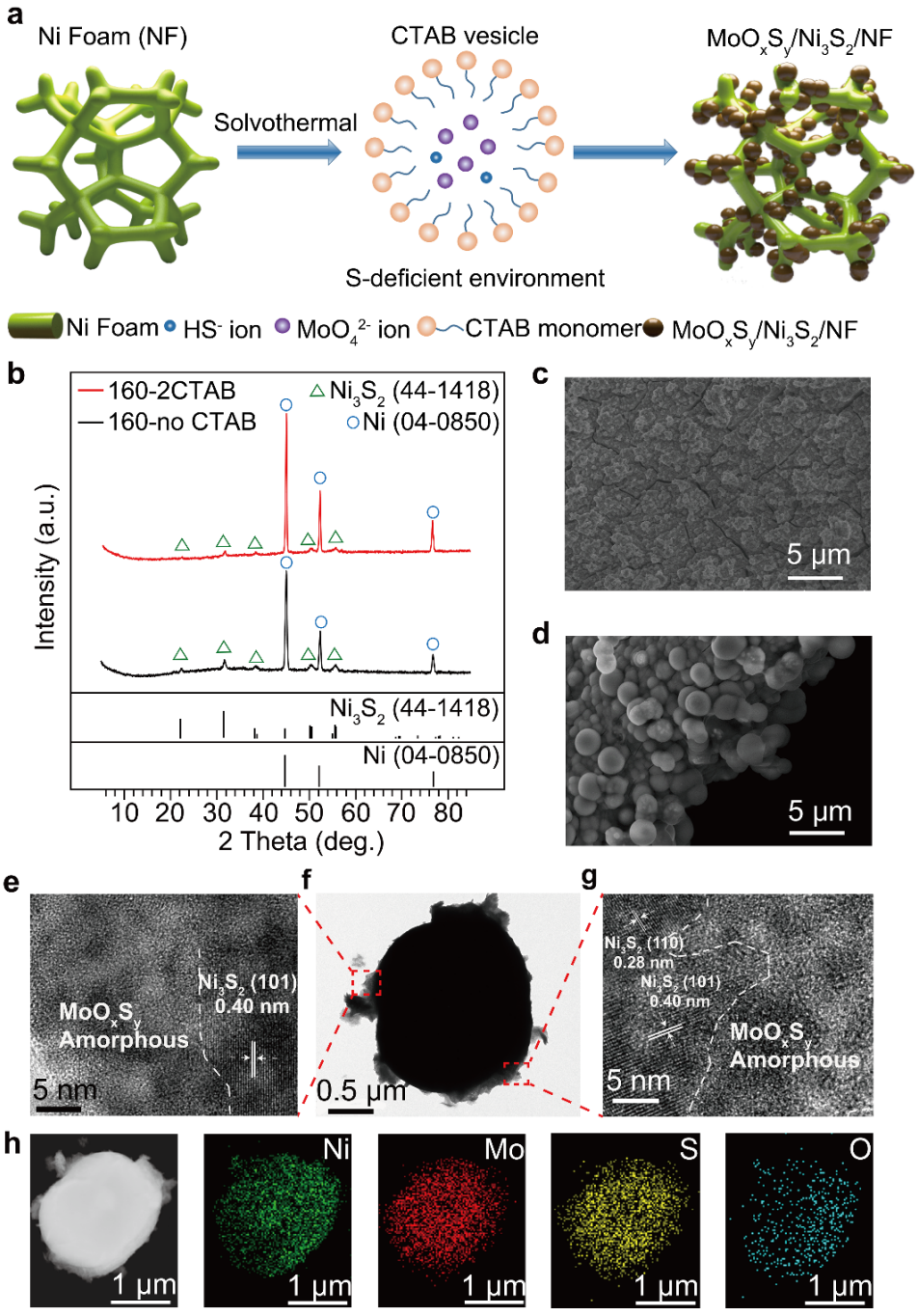

Figure 1. Formation mechanism and structure characterization. (a) Schematic

illustration of formation mechanism of MoO_xS_y/Ni_3S_2/NF *via* a CTAB-assisted solvothermal reaction (160-2CTAB). (b) XRD patterns, Bragg diffraction peaks are assigned to the specific components of the hierarchical composite. MoO_xS_y in 160-2CTAB is amorphous and shows no XRD peaks. (c) SEM image of 160-no CTAB. (d) SEM image of 160-2CTAB. (e, g) HRTEM images in selected area of (f). (f) TEM image of 160-2CTAB microsphere scratched from NF. (h) HAAD FSTEM image of 160-2CTAB microsphere and elemental mapping of Ni, Mo, S, and O.

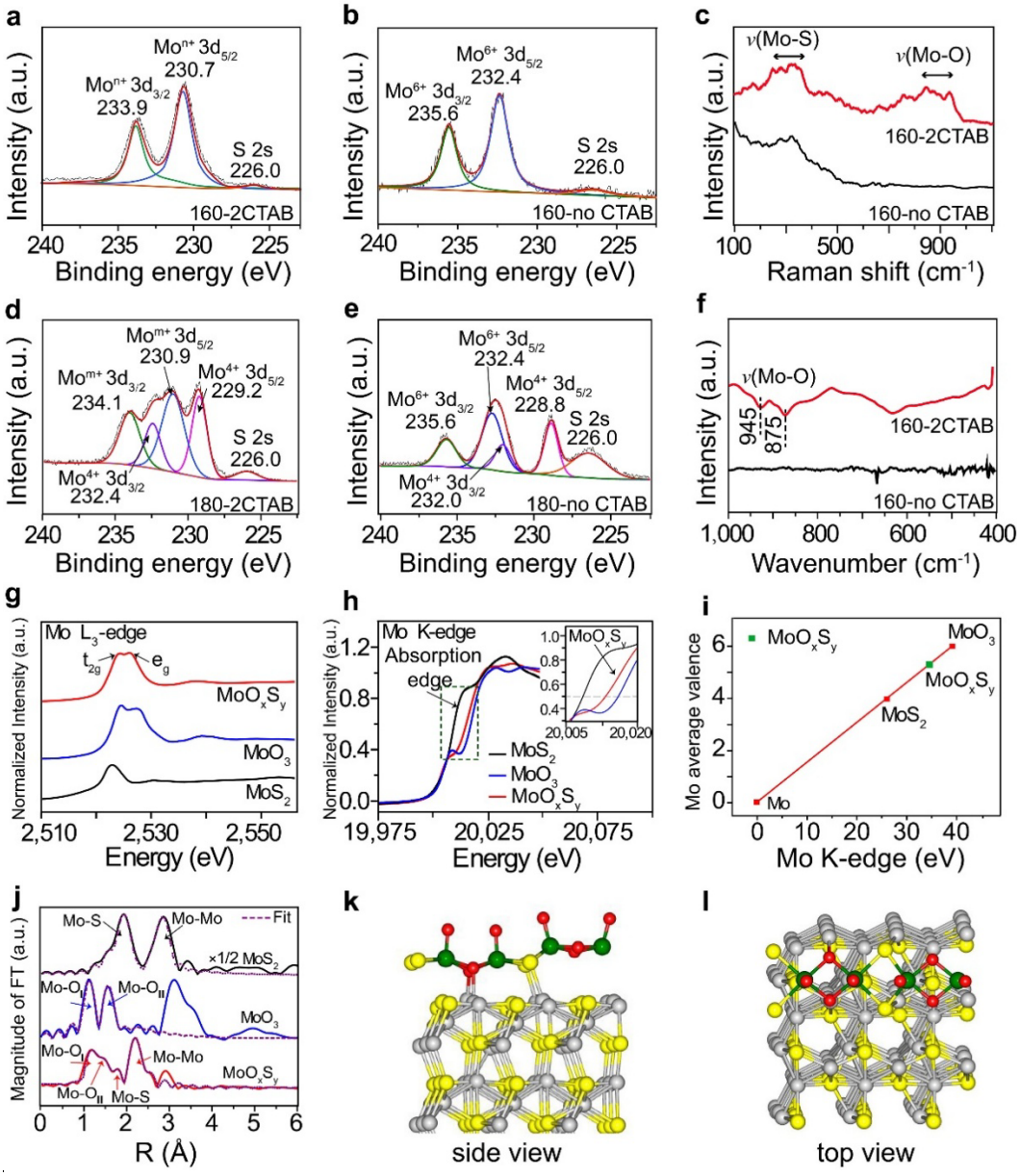

Figure 2. Effects of temperature and CTAB on material structure and optimization model based on coordination environment analysis. (a, b) X-ray photoelectron spectra with deconvolution of Mo 3d of 160-2CTAB and 160-no CTAB. (c) Raman spectra of 160-2CTAB and 160-no CTAB. (d, e) X-ray photoelectron spectra with deconvolution

of Mo 3d of 180-2CTAB and 180-no CTAB. (f) IR spectra of 160-2CTAB and 160-no CTAB. (g) Mo L_3-edge XANES of MoO_xS_y, MoO_3 and MoS_2. (h) Mo K-edge XANES of MoO_xS_y, MoO_3, and MoS_2, the insert shows an expanded view of the edge region. (i) Mo average valence of MoO_xS_y obtained through linear fitting. (j) FT-EXAFS with experimental and fitted spectra of Mo K-edge of MoO_xS_y, MoO_3 and MoS_2. DFT optimized structure model $[Mo_4O_8S_4]$@Ni_3S_2(101) for MoO_xS_y/Ni_3S_2 in (k) side view and (l) top view. Symbols of atoms are as follows: Mo in green, S in yellow, O in red, and Ni in gray.

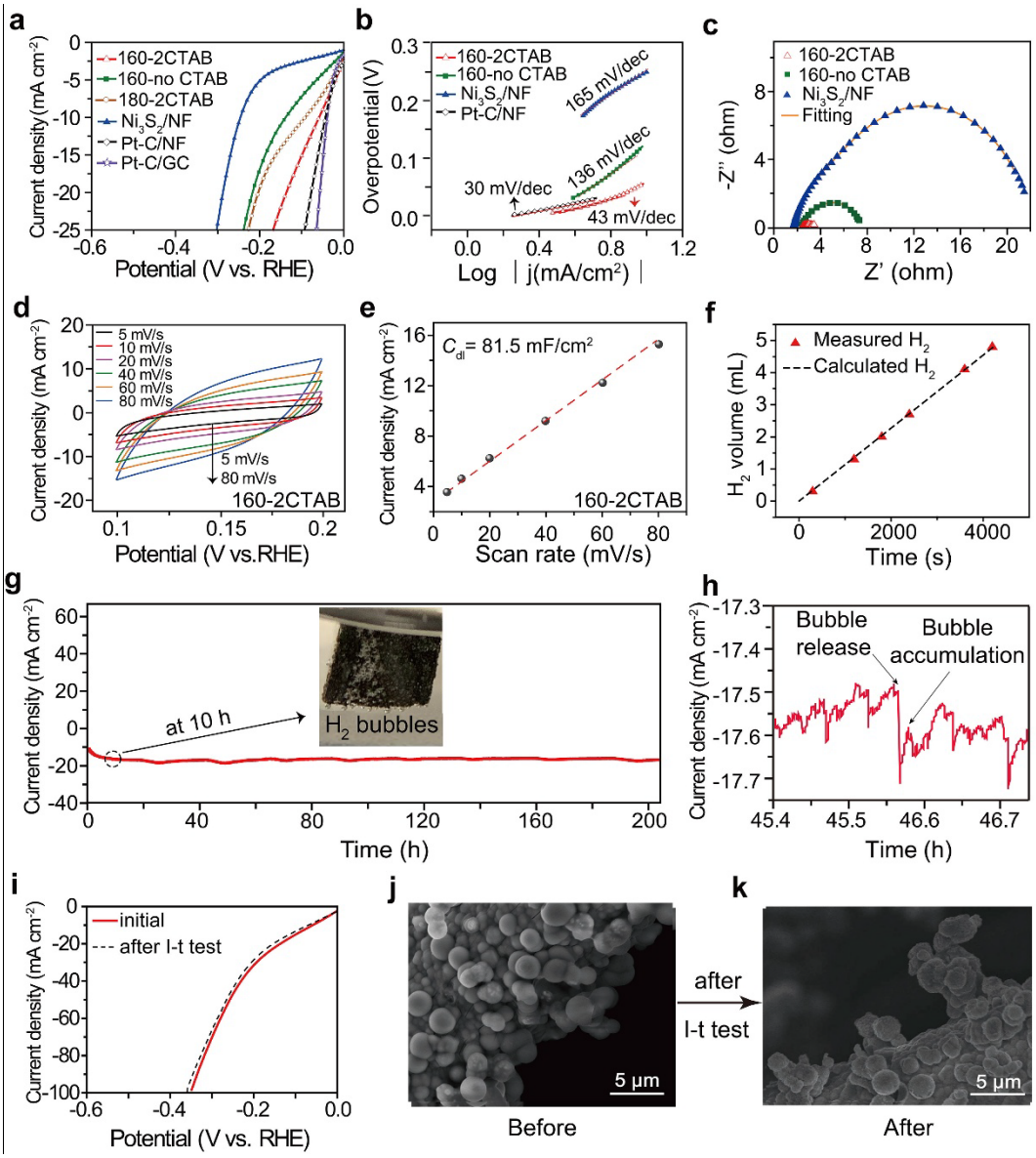

Figure 3. Electrocatalysis performance. (a) Polarization curves of 160-2CTAB, 160-no CTAB, Ni_3S_2/NF, 180-2CTAB, Pt-C/NF and Pt-C/GC. (b) Tafel slopes of 160-2CTAB, 160-no CTAB, Ni_3S_2/NF and Pt-C/NF derived from polarization curves. (c) Nyquist plots of 160-2CTAB, 160-no CTAB and Ni_3S_2/NF at -250 mV vs. RHE measured from EIS in the frequency range from 10^5 Hz to 0.01 Hz. (d) Cyclic voltammograms at

various scan rates of 5, 10, 20, 40, 60 and 80 mV s^{-1} for 160-2CTAB from 0.1 to 0.2 V vs. RHE. (e) Plots of current density as a function of scan rates for 160-2CTAB. (f) Measured and calculated volume of H_2 as a function of time for 160-2CTAB. (g) Chronoamperometric curve of 160-2CTAB at a constant applied potential of -120 mV vs. RHE. Inset of photograph shows the generation of H_2 bubbles on the electrode at 10 h during the stability test. (h) Partial enlargement of (g) plot. (i) Polarization curves before and after 200 h I-t test of 160-2CTAB. (j) SEM images of 160-2CTAB before the I-t test. (k) SEM image of 160-2CTAB after I-t test.

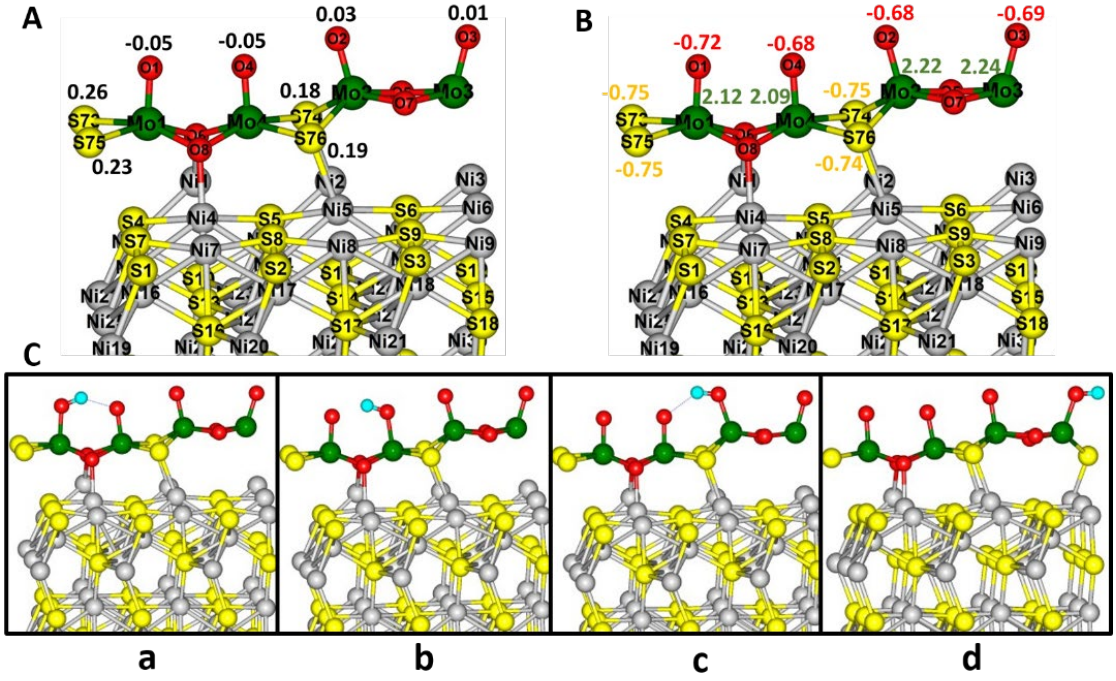

Figure 4. Structure models for MoO_xS_y/Ni_3S_2 and HER active sites. (A) DFT optimized structure model of $[Mo_4O_8S_4]@Ni_3S_2(101)$ and calculated HER reaction free energies (eV) on double bonded O and bridging S active sites at the potential U = 0 V relative to standard hydrogen electrode at pH = 0. (B) DFT calculated Bader charges (*e*) on atoms in MoO_xS_y. (C) Optimized structures of H* at different M=O binding sites (a-d). Symbols for atoms: Mo in green, S in yellow, O in red, Ni in gray, and H in blue.

Table 1. Comparison of HER activity of MoO_xS_y/Ni_3S_2/NF (160-2CTAB) with reported Mo-based electrocatalysts.

Electrolyte	Electrocatalysts	η_{10} (mV)	References
0.5 M H_2SO_4	**MoO_xS_y/Ni_3S_2/NF**	**58**	**This work**
	defect-rich MoS_2	~180	Adv. Mater. 2013.[54]
	double gyroid MoS_2	206	Nat. Mater. 2012.[11]
	wet-chemical amorphous MoS_x	200	ACS Catal. 2012.[55]
	$[Mo_3S_{13}]^{2-}$/graphite paper	174	Nat. Chem. 2014.[56]
	Ni doped MoS_3	158	Chem. Sci. 2012.[58]
	Pt-MoS_x	95	ACS Appl. Mater. Interfaces 2018.[59]
	$MoWS_x/BPE_{anodic}$	278	ACS Appl. Mater. Interfaces 2017.[60]
	Au-MoS_2	120	J. Am. Chem. Soc. 2015.[61]
	P-doped MoS_2	43	ACS Energy Lett. 2017.[65]
	MoS_2/hydrogenated graphene	124	ACS Catal. 2018.[62]
	1T MoS_2 nanosheets	187	J. Am. Chem. Soc. 2013.[63]
	MoS_x/graphene/NF	~150	Adv. Mater. 2013.[24]
0.1 M $HClO_4$	$CoMoS_x$	>200	Nat. Mater. 2016.[64]

Table 2. Comparison of HER activity of MoO_xS_y/Ni_3S_2/NF (160-2CTAB) with Ni-based electrocatalysts.

Electrolyte	Electrocatalysts	η_{10} (mV)	References
0.5 M H_2SO_4	**MoO_xS_y/Ni_3S_2/NF**	**58**	**This work**
	Ni_3S_2/Ni_2P	107	ChemCatChem 2018.[66]
	Sn-doped Ni_3S_2	201	ChemElectroChem 2017.[67]
	Ni_2P/NF	106	Int. J. Electrochem. Sci. 2020.[68]
	CoP_3/Ni_2P	115	J. Mater. Chem. A 2018.[69]
	MOF-Ni_2P	158	Appl. Mater. Interfaces 2017. [70]
	$NiSe_2$@NC	161	Int. J Energy Res. 2021.[71]
	$NiSe_2$@NG-140	201	ACS Sustain. Chem. Eng. 2019. [74]
	$NiSe_2$/Ni	~143	Nano Energy 2016. [73]

For Table of Contents Only